Interdecadal Amplitude Modulation of El Nino/Southern Oscillation and its Impacts on Tropical Pacific Decadal Variability

Tomomichi Ogata[1, #]

Shang-Ping Xie[1, 2, @]

Andrew Wittenberg[3]

De-Zheng Sun[4]

[1]International Pacific Research Center, Honolulu, Hawaii, USA

[2]Department of Meteorology, University of Hawaii at Manoa, Honolulu, Hawaii, USA

[3]Geophysical Fluid Dynamics Laboratory, Princeton, New Jersey, USA

[4]University of Colorado, and NOAA/Earth System Research Laboratory, Boulder, Colorado, USA

Submitted to J. Climate

(Present affiliation)

[#]Graduate School of Life and Environmental Sciences, University of Tsukuba, Tsukuba, Japan

[@]Scripps Institution of Oceanography, University of California at San Diego, La Jolla, California, USA

Abstract

The amplitude of El Nino/Southern Oscillation (ENSO) displays pronounced interdecadal modulations in observations. The mechanisms for the amplitude modulation are investigated using a 2000-year pre-industrial control integration from the Geophysical Fluid Dynamics Laboratory Climate Model 2.1 (CM2.1). ENSO amplitude modulation is highly correlated with the second empirical orthogonal function (EOF) mode of tropical Pacific decadal variability (TPDV), which features equatorial zonal dipoles in sea surface temperature (SST) and subsurface temperature along the thermocline. Experiments with an ocean general circulation model indicate that both interannual and decadal-scale wind variability are required to generate decadal-scale tropical Pacific temperature anomalies at the sea surface and along the thermocline. Even a purely interannual and sinusoidal wind forcing can produce substantial decadal-scale effects in the equatorial Pacific, with SST cooling in the west, subsurface warming along the thermocline, and enhanced upper-ocean stratification in the east. A mechanism is proposed by which ENSO's residual effects could serve to alter subsequent ENSO stability, possibly contributing to long-lasting epochs of extreme ENSO behavior via a coupled feedback with TPDV.

1. Introduction

El-Nino/Southern Oscillation (ENSO) is the dominant mode of interannual climate variability, affecting tropical atmospheric variability such as the Walker circulation (Walker 1923) and global climate through atmospheric teleconnections (Horel and Wallace 1981). Long-term changes in ENSO characteristics have received much attention (Fedorov and Philander 2001, Wittenberg 2002, Wang and An 2002, Wittenberg 2004, Ashok et al. 2007, Kao and Yu 2009, Wittenberg 2009, Vecchi and Wittenberg 2010, Collins et al. 2010, McPhaden et al. 2011). McPhaden et al. (2011) reported that the recent increased occurrence of central Pacific El Nino is associated with anomalously shoaled (deepened) thermocline depth in the eastern (western) equatorial Pacific.

In observations, ENSO amplitude has changed on interdecadal timescales (Li et al. 2011, Chowdary et al. 2012) and such interdecadal ENSO modulation affects the global climate. Recent studies show that the interdecadal modulations of ENSO flavors and amplitude affect its global teleconnections (Ashok et al. 2007, Kug et al. 2010, Xie et al. 2010, Chowdary et al. 2012). For example, Xie et al. (2010) reported that interannual variability of the summer subtropical high in the northwestern Pacific is generated by ENSO through the Indian Ocean “capacitor” effect after the late 1970’s regime shift, but such a teleconnection mechanism does not work before the regime shift when ENSO amplitude is weak. In a long (1000 years) integration with a coupled general circulation model (CGCM), Rodgers et al. (2004) pointed out that the ENSO amplitude significantly fluctuates on interdecadal timescales. They found that the interdecadal ENSO variability co-varies with the background mean state referred to as the tropical Pacific decadal variability (TPDV). The time series of the TPDV defined as the first EOF mode of the 11-

year low-passed variability of 20°C isotherm depth along the equatorial Pacific and resembles the regressed pattern based on an ENSO variance index. Such TPDV mode displays significant SST variability with a zonal dipole pattern along the equator. This suggests that the thermocline feedback is involved in the TPDV mode. Subsequent studies using different CGCMs report similar results (e.g. Timmerman 2003, Wittenberg 2009, Choi et al. 2009), though the ability of CGCMs to capture the processes relevant to ENSO is still evolving (Guilyardi et al. 2009, 2012). More recent studies derive similar results using the second EOF mode of decadal SST variability in the tropical Pacific (Sun and Yu 2009, Yu and Kim 2011).

Studies of relationships between the mean state and ENSO amplitude modulation can be classified to two types: those examining the response of ENSO amplitude to various mean state changes under stochastic forcing in a hierarchy of coupled models (e.g. Kirtman and Schopf 1998, Wittenberg 2002, Fang et al. 2008, Burgman et al. 2008, Anderson et al. 2009, DiNezio et al. 2012), and those exploring the interactive relationship between ENSO amplitude and TPDV (e.g. Rodgers et al. 2004, Schopf and Burgman 2006, Wittenberg 2009, Choi et al. 2009, Watanabe and Wittenberg 2012, Watanabe et al. 2012). In the latter group, the nonlinearity of ENSO is deemed a major driver of TPDV. In particular, the asymmetry between strong El-Nino and weak La-Nina increases during strong ENSO epochs and imprints on the background mean state as a residual mean. More recently, Liang et al. (2012) shows the ENSO rectification on mean state using a recharge-discharge model. Such ENSO rectification is consistent with previous studies using OGCM (Sun and Zhang 2006, Sun 2010), suggesting that such a rectification mechanism may be applied to the TPDV formation.

The interactive dynamics linking the TPDV and ENSO amplitude modulation, especially how ENSO amplitude modulation affects TPDV, is not completely understood. Given the similarity between the residual mean of composite El-Nino/La-Nina events and the TPDV, previous studies have argued for ENSO-driven SST skewness imprinting on the mean state (e.g. Rodgers et al. 2004, Wittenberg et al. 2009, Choi et al. 2009), but the formation mechanisms for the TPDV have not been quantified in ocean and atmospheric GCMs.

The present study investigates the effects of ENSO variance on decadal variations in the mean state, based on a 2000-year long integration with a state-of-the-art coupled GCM (Wittenberg 2009). As there are numerous studies of how mean state changes affect ENSO, here we focus on how ENSO variance modulations rectify onto the mean state. We decompose the atmospheric variability in the coupled GCM into interannual and longer components and force an ocean GCM with these components of wind forcing together and separately. Our results show that rectified effects of the interannual wind forcing contribute substantially to decadal variations in the ocean mean state. Specifically, elevated ENSO variance strengthens the upper-ocean stratification in isothermal coordinates and hence potentially thermocline feedback. Similar results are obtained using an idealized wind cycle that is sinusoidal in time, suggesting the importance of ENSO wind variance, instead of the skewness, for the rectification on the mean state.

The rest of the paper is organized as follows. Section 2 describes datasets used in this study. Section 3 shows that the interdecadal ENSO modulation is related to the TPDV in a long CGCM simulation. Section 4 presents the importance of ENSO forcing and its asymmetric response for the TPDV formation using OGCM sensitivity experiments.

Section 5 examines the mean state change of thermocline shape in the eastern equatorial Pacific. Section 6 is a summary with discussions.

2. Data and Models

This study analyzes observational data and simulations from coupled and ocean GCMs. For observations, we use the Extended Reconstructed SST (ERSST) product (Smith et al. 2008) for 1948-2009 on a 2.5 degree grid, and 10m wind from the National Center for Environmental Prediction and National Center for Atmospheric Research (NCEP/NCAR) reanalysis (Kalnay et al. 1996) for 1948-2009 on a T63 (about 1.875 degree) Gaussian grid.

A 2000-year integration with the Geophysical Fluid Dynamics Laboratory Climate Model version 2.1 (GFDL-CM2.1; Delworth et al. 2006; Wittenberg et al. 2006; Wittenberg 2009) is analyzed. CM2.1 consists of ocean, atmosphere, land components and their coupler. The oceanic component is based on the Modular Ocean Model version 4 (MOM4) code (Griffies et al. 2005; Gnanadesikan et al. 2006). The horizontal resolution is 1° in longitude and 1° in latitude with enhanced tropical resolution (1/3° within 10° of the equator). There are 50 vertical levels with a constant spacing of 10m in the top 220m. Isopycnal mixing of tracers and layer thickness is based on the formulation by Gent and McWilliams (1990), Griffies et al. (1998), and Griffies (1998). The mixed-layer is represented by the K-profile parameterization (KPP) vertical mixing (Large et al. 1994). The atmospheric component is the AM2.1 atmosphere model (GFDL Global Atmospheric Model Development Team: GAMDT 2004). It consists of a finite volume dynamical core (Lin 2004) with 24 vertical levels, 2° latitude by 2.5° longitude grid spacing, and a relaxed Arakawa-Schubert convection scheme (Moorthi and Suarez 1992). The coupled simulation lasts for 2220 years with constant pre-industrial (year 1860) anthropogenic forcing. The last 2000 years of output is used for analysis. The atmosphere, ocean, land and sea ice exchange fluxes every two hours and no flux adjustments are employed. Figure 1 compares El Niño composites of SST and surface wind anomalies between CM2.1 (246 events) and ERSST/NCEP observations (19 events). Composite events are picked up when Nino-3 SSTA during December-February exceeds 1 σ . CM2.1 captures observed seasonal evolution of ENSO, which develops in boreal fall to summer, matures in fall to winter and rapidly decays in spring. The simulation overestimates ENSO amplitude compared to observations. CM2.1 simulates a realistic mean state, ENSO, and its seasonality (e.g. Wittenberg et al. 2006, Wittenberg 2009, Kug et al. 2010). The long-term simulation improves statistical significance of ENSO and TPDV properties.

In order to investigate the role of ocean dynamics, we conduct sensitivity experiments with the Modular Ocean Model version 3 (MOM3) (Pacanowski and Griffies 1999). The model covers a near global domain from 65°S to 65°N. The model resolution is 2.5 degree in zonal, 0.5 degree from 15°S to 15°N with a gradual increase to 2 degree in meridional, and 25 levels in vertical (10 m intervals in the upper 100 m). The vertical mixing parameterization of Pacanowski and Philander (1981) is adopted. Surface boundary conditions are calculated from the bulk formula of Rosati and Miyakoda (1988) except that surface air temperature is assumed as SST-2°C. This model has been used in several studies, capable of realistic simulations in the tropics (Tozuka et al. 2010, Morioka et al. 2011). The OGCM is spun up for 28 years under the monthly CM2.1 surface climatology. Appendix A compares MOM3 and MOM4 simulations. The results presented here are qualitatively insensitive to the choice of ocean GCMs.

3. Interdecadal ENSO modulation and TPDV

Figure 2a shows the 20-year running standard deviation of the high-passed Nino-3 variability for the last 1000 years in CM2.1. In this study, ENSO is represented by Dec-Feb Nino-3 SST (210-260°E, 5°S-5°N), filtered with a 10-year high-pass filter. The ENSO amplitude fluctuates on interdecadal timescales, ranging from 0.6 to 2.0 °C. The interdecadal ENSO amplitude modulation is associated with the background mean state change. Figure 3 shows the regression pattern of 20 year low-passed ENSO variance onto the 20-year low-passed SST and SSH anomaly fields. There is a significant zonal dipole pattern over the tropical Pacific; the eastern (western) Pacific is anomalously cool (warm) during strong ENSO epochs. This interdecadal SST variability is associated with the thermocline/SSH variability with a flattened thermocline during strong ENSO periods. Previous studies (e.g. Jin 1998, Rodgers et al. 2004, Choi et al. 2009) also reported that the cold-tongue warming, the relaxed easterly winds and a flattened thermocline intensify the ENSO amplitude and favor longer ENSO periods.

These interdecadal ENSO background state changes represent a major mode of TPDV. To obtain the TPDV modes, the empirical orthogonal function (EOF) analysis is performed for the 20-year low-passed SST field over the tropical Pacific (120-280°E, 20°S-20°N). The first TPDV mode in Figure 4a shows a basin-wide pattern over the tropical Pacific. The spatial pattern of surface heat flux anomalies and their relationship to SST are less coherent compared to the second TPDV mode over the tropical Pacific, suggesting that the first TPDV mode is generated by the complicated ocean and atmospheric dynamics (Fig. 4a). The second TPDV mode features a zonal dipole pattern over the tropical Pacific warming in the east and cooling in the west during the positive TPDV phase. It is associated with large thermocline variability (Fig. 4b). The regressed SSH field shows a significant zonal dipole pattern. At the positive TPDV phase, anomalous westerly winds blow over the central equatorial Pacific and the SSH dipole pattern represents a flattened thermocline. Surface heat flux anomaly tends to cool (warm) the ocean in the region of positive (negative) SST anomalies. This suggests that the subsurface oceanic processes are the main driver in the second TPDV mode. Hereafter, TPDV simply refers to the second mode for brevity.

The spatial similarity between mean state variability associated with the ENSO amplitude modulation and the TPDV (Figs. 3 and Fig. 4b) suggests a close relationship between them. Figure 2b shows the time series of the second TPDV mode for the last 1000 years in CM2.1. Correlation with the ENSO amplitude time series is obvious. Correlation coefficient between these two time series is 0.84, above 95% significance level. Such similarity between the ENSO amplitude and the TPDV can be seen in other CGCMs (e.g. Rodgers et al. 2004, Choi et al. 2009), but these previous studies emphasized the importance of ENSO asymmetry. In CM2.1, correlation coefficient between 20-year sliding Nino-3 skewness and standard deviation is much lower at 0.50, but remains above 95% significance level.

4. Contribution of ENSO for TPDV formation

a. OGCM experiments with CM2.1 forcing

To quantify the contribution of intraseasonal variability (ISV), ENSO and decadal variability (DV) forcing, OGCM experiments with “realistic” CM2.1 forcing are executed. We choose 5 strong ENSO/positive TPDV epochs (year 901-920, 991-1010, 1641-1660, 1731-1750 and 1861-1880) and 5 weak ENSO/negative TPDV epochs (year 351-370, 1161-1180, 1681-1700, 1811-1830 and 1961-1980). Epochs are chosen where both time series of the second TPDV and the 20-year running standard deviation of Nino-3 SSTA exceeds $\pm 1\sigma$. Surface boundary conditions are calculated from the bulk formula of Rosati and Miyakoda (1988) using climatological surface atmospheric field except that surface air temperature is assumed as SST-2°C. From the CM2.1 simulation, wind stress forcing for each 20 years long segment is decomposed into three components: ISV (3-month high-pass), ENSO (3-month to 10-year band-pass anomaly) and DV (10-year low-pass anomaly). Then three OGCM runs are performed: ISV+ENSO+DV, ENSO+DV and DV runs. The monthly climatology is included. Contribution of ISV, ENSO and DV to the TPDV is quantified by comparing the difference in each run between “strong ENSO/positive TPDV” and “weak ENSO/negative TPDV” epochs (hereafter we define it as “anomaly”). These are five 20-year epochs for each phase, and composite difference fields between the positive and negative phases are presented.

Figure 5 shows the SSH anomalies in DV+ENSO+ISV and DV runs. SSH response in the DV+ENSO+ISV run has a similar dipole pattern, negative (positive) in the western (eastern) Pacific. In the DV run, on the other hand, the east-west SSH contrast weakens, indicating a significant direct contribution of ENSO to the SSH mean state as represented by the difference between DV+ENSO+ISV and DV runs (Fig. 5c).

The ENSO effect is more clearly seen in the thermal structure on the equator. Figure 6 shows the temperature response on the equator in OGCM runs. Anomalies in the

DV+ENSO+ISV run (Fig. 6b) show a dipole pattern with cooling (warming) in the west (east), similar to the second TPDV mode (Fig. 6a). In contrast, the DV only forcing could not reproduce important features of the second TPDV mode (Fig. 6c), including the mixed layer cooling in the west and the thermocline warming in the east.

In the OGCM experiments, the direct ENSO contribution can be evaluated by taking a difference between the DV+ENSO and DV forcing response. Figs. 5c and 6d show the contribution of ENSO forcing to the TPDV. In SSH, ENSO forcing enhances the zonal dipole pattern by 2 cm in east-west difference (Fig. 5c). Thermal structure on the equator (Fig. 6d) exhibits the warming along the 20°C isotherm slope and surface cooling in the western basin (140-200°E). The ENSO rectification effect is similar to the result of Sun (2010, Plate 5) based on a different OGCM. With a relaxation of the east-west thermocline slope, Bjerknes feedback may generate westerly wind anomaly in response to the rectified SST (Liang et al. 2012).

Compared to ENSO forcing, the contribution of ISV forcing to the TPDV is weak (figure not shown). The ISV effect is not so different between strong ENSO/positive TPDV and weak ENSO/negative TPDV epochs, in deviation from previous studies about the ISV effect on the mean state using OGCM (e.g. Kessler and Kleeman 2000, Suzuki and Takeuchi 2000). High correlation (~0.48, above 95% significance level) between ISV variance and Nino-3 on interannual timescales is consistent with previous studies of state dependent subseasonal noise on ENSO (Gebbie et al. 2007), while correlation between ISV variance and Nino-3 variance on decadal timescales drops to 0.30. This may imply that the impact of subseasonal noise on the TPDV is less important than that to the ENSO. It should be noted that monthly mean wind forcing we use smooths out such subseasonal variability and so its effect in our OGCM experiments may be underestimated.

b. OGCM experiments with periodic forcing

The previous section showed that ENSO forcing is important to generate the TPDV. To illustrate the importance of ENSO forcing, OGCM experiments are also performed by using sinusoidal wind forcing with a 2-year periodicity (2yrENSO run). The amplitude of the wind stress anomalies (0.2 dyn/cm^2) is comparable to the 20-yr sliding standard deviation of interannual variability (IAV: 10-yr high-passed zonal wind stress) over the central Pacific (5°S-5°N, 160-210°E) in GFDL-CM2.1. The spatial pattern of wind stress anomalies is assumed as a Gaussian-shape structure centered on the equator as shown in Figure 7. The structure function is expressed as:

$$f(x,y,t)=\tau_0\times\exp\left(-\left(\frac{x-x_0}{\Delta x}\right)^2-\left(\frac{y}{\Delta y}\right)^2\right)\times\cos\left(2\pi\frac{t}{24}\right) \quad (1),$$

where τ_0=0.2 dyn/cm^2, Δx=30°, Δy=10°. x, y, t are longitude, latitude and month. Following observations and simulated results, the peak of westerly variability is set in January. In the 2yrENSO run, OGCM is integrated for 20 years with the periodic wind stress anomalies. The last two cycles (4 years) are used for analysis by comparing the difference between the 2yrENSO run and climatological run (CTRL run). We note that the wind stress anomalies are symmetric in time between the westerly and easterly phases. Wind speed anomalies are not applied in surface turbulent heat flux calculations.

Figure 8 shows the SSH and temperature difference between the 2yrENSO and CTRL runs. SSH and temperature pattern in the idealized experiment is quite similar to the experiment using the CM2.1 forcing (Fig. 5c and 6d). In particular, the zonal dipole SSH response, the surface cooling on the edge of the cold tongue and warming along the 20°C isotherm are common between the CM2.1 and the idealized forcing runs. This idealized experiment illustrates that the sinusoidal forcing without asymmetry can generate the mean state change. We note that Figs. 6d and 8b show some similarity with results from an idealized 2-dimensional warm-pool displacement by Schopf and Burgman (2006). The similarity suggests that the adiabatic effect is important to form the ENSO rectification despite that their model is highly idealized (e.g., the warm water volume is not conservative on the equator).

Next we investigate the cause of the mean state changes. First the cooling on the west edge of the cold tongue over 140-200°E is investigated. Figure 9 compares the near-surface temperature and current anomalies at La-Nina and El-Nino phases. In addition to the significant response in the cold tongue around 80-140°W, significant temperature response exists on the edge of the cold tongue in phase. Westward (eastward) current anomalies occur during La-Nina (El-Nino). Such anomalous temperature and current responses form a net cooling effect through the nonlinear zonal advection ($-u'*dT'/dx$). As a result, a mean cooling response is generated by the zonal advection on the west edge of the cold tongue.

The net warming along the climatological depth of the 20°C isotherm forms by different mechanisms. Figure 10 shows the temperature response on the equator during the cold to warm phase transition (left) and the warm to cold phase transition (right). In the left panels, warm subsurface temperature anomalies are generated in the western Pacific at La-Nina peak and shows an apparent eastward propagation along the 20°C isotherm with the relaxation of the easterly wind anomalies. In the right panels, cold temperature anomalies are generated in the western Pacific at El-Nino peak and then propagate eastward. The cold temperature anomalies propagate above the climatological 20°C isotherm and seem to be damped in the propagation. The eastward propagating warm signals along 20°C isotherm (1.5-2°C) on the left panels seem stronger than the cold signals on the right panels (1-1.5°C). The asymmetry of the propagation depth for cold and warm signals affect the strength of the signals, and the asymmetric signals are projected onto the mean state along the 20°C isotherm.

To illustrate that the propagation depth affects the strength of temperature signals, Figure 11 shows the longitude-depth sections of vertical temperature gradient (*dT/dz*) and Richardson number, important parameters for vertical mixing. Large (small) *dT/dz* and Richardson number indicate small (large) vertical mixing coefficient. Large *dT/dz* and Richardson number spread along the 20°C isotherm and decrease sharply above the thermocline. The warm signals in Fig. 10 are kept strong and propagate along the 20°C isotherm where the vertical mixing is inactive while the cold signals dissipate rapidly and propagate above 20°C isotherm where the vertical mixing is active. Appendix B presents heat budget, illustrating roles of advection and vertical mixing.

We recognize that wind anomalies are not symmetric between El-Nino and La-Nina, both in magnitude and duration (Ohba and Ueda 2009, Okumura et al. 2011, Ohba 2012). Our idealized wind forcing is designed to illustrate the variance effect, instead of ENSO asymmetry effect emphasized in previous studies. We have also run an OGCM experiment with 4-year periodic forcing. The result is qualitatively similar but the rectification on the mean is slightly weaker than in the 2-year case at the same forcing magnitude. This implies that the basin-wide oceanic response in the tropical Pacific is somewhat sensitive to the forcing period. Other factors such as tropical instability waves, meridional heat transport by Ekman divergence, and surface heat flux also may be important in the real world. While TIWs are weak in CM2.1, the heat convergence by TIWs may contribute to the asymmetry of ENSO (An 2008, An 2009). Sun et al. (2012) reports a TIW effect on ENSO rectification using an OGCM, showing that the TIW-induced equatorial cooling improves the consistency with observations. ENSO asymmetry may be another factor for the rectification. During epochs of large (small) ENSO amplitude El-Nino to La-Nina transitions take place fast (slow) in both observations and CM2.1 (Ohba 2012). Strong El-Nino (weak La-Nina) during large ENSO amplitude epochs may strengthen the warming signal near the thermocline. The similarity in ENSO rectification between runs with realistic CM2.1 forcing (including asymmetry) and idealized 2-yr ENSO forcing (without asymmetry) suggests the importance of ENSO variance effect. However this does not rule out the possibility of ENSO asymmetry effect.

5. ENSO rectification on stratification

Figure 12 shows the response of temperature to periodic vertical displacements of the thermocline that maintains the same vertical temperature profile. This results in an Eulerian mean dipole in the vertical, warming in the lower and cooling in the upper thermocline, smoothing out the Eulerian time-mean temperature gradient (Schopf and Burgman 2006). By definition, the adiabatic displacements of the thermocline do not alter stratification on isothermal coordinates. The effect of such adiabatic thermocline displacements on thermocline feedback and ENSO growth is unclear. Strong mixing in the mixed layer destroys the negative pole of the Eulerian mean temperature dipole, leaving behind the warming in the lower thermocline as is observed in CM2.1 and OGCM experiments. To avoid the smoothing of the thermocline in the Eulerian mean, we propose an isothermal-coordinate perspective. Time-mean *dT/dz* in Fig. 12, in isothermal coordinates, is unchanged from the snapshot, while that on z coordinates is different from the snapshot. This gives a reason why a view from isothermal coordinates is more suitable to capture the “mean” thermocline shape.

Figure 13 shows the *dT/dz* difference in isothermal coordinates in CM2.1 between “strong ENSO/positive TPDV” and “weak ENSO/negative TPDV” epochs at 0°N110°W. First the monthly snapshot of *dT/dz* in isothermal coordinates is calculated, and then its climatology is derived. There is a significant difference in *dT/dz* in the upper layer (above 16°C) for October-January. The stratification (*dT/dz*) during “strong ENSO/positive TPDV” epochs is stronger than during “weak ENSO/negative TPDV” epochs by about 0.02°C/m. *dT/dz* is generally similar during other seasons. A stronger *dT/dz* during “strong ENSO/positive TPDV” epochs may lead to a more effective thermocline feedback and ENSO activity in the cold tongue region.

Similar changes of the thermocline shape can be seen in the idealized experiment. Figure 14 shows the *dT/dz* difference in isothermal coordinates between 2yrENSO and CTRL runs at 0°N110°W. Similar to Fig. 13, there is a significant difference in *dT/dz* in the upper layer (above 16-18°C) during boreal fall to spring. *dT/dz* in the 2yrENSO run is twice as large as in the CTRL run during this period, suggesting that the ENSO forcing can intensify *dT/dz* near the surface in the cold tongue region.

According to the linear stability analysis (Fedorov and Philander 2002), vertical advection is important for thermocline feedback. The vertical advection term in the mixed layer temperature equation may be represented as:

$$-\bar{w}\frac{T' - T'_{sub}}{H_{mix}} \approx -\frac{\bar{w}}{H_{mix}}\left(T' - \frac{d\bar{T}}{dz}h'\right) = -\mu T' + \kappa h' \qquad (2),$$

where $\bar{w}$ the mean vertical velocity, H_{mix} the mixed layer depth, T' the mixed temperature anomaly, T'_{sub} the subsurface temperature anomaly, $d\bar{T}/dz$ the climatological subsurface temperature gradient, and h' the thermocline depth anomaly. Thus a stronger *dT/dz* increases the SST sensitivity to thermocline displacement, which in turn may help to strengthen ENSO activity through thermocline feedback. Our results (Figs. 13, 14) indicate that enhanced ENSO activity in turn strengthens *dT/dz*. This relationship between ENSO activity and *dT/dz* forms a positive feedback loop. Regression coefficient between SST and SSH over Nino-3 region, *R(T', h')*, is a good indicator for thermocline feedback. *R(T', h')* in 20-year running mean is highly correlated with the ENSO amplitude modulation (Corr=0.55) above 95% significance level. This suggests that the stronger (weaker) thermocline feedback coefficient [κ in Eq. (2)] increases (decreases) ENSO amplitude. On the other hand, it should be noted that other process (zonal advection, surface heat flux etc.) are also important and the reality is more complicated.

6. Summary

We have investigated the interdecadal modulation of ENSO amplitude and its relationship to the TPDV. From a 2000-year integration of CM2.1, interdecadal ENSO amplitude modulation is correlated with the second TPDV mode. From OGCM experiments, we show that the second TPDV mode is generated by not only the decadal wind forcing but also interannual forcing. In particular, the IAV wind rectification warms the thermocline along the 20°C isotherm in the eastern Pacific. In the mixed layer, enhanced IAV leads to a net warming in the east and a net cooling in the west half of the basin. In an isothermal coordinate view, upper layer stratification (*dT/dz*) intensifies during "strong ENSO/positive TPDV" epochs, and the idealized experiment suggests that the sharpened thermocline is due to the enhanced ENSO forcing.

Although the broad pattern of the rectification effect resembles what is identified before (Sun and Zhang 2006, Sun 2010), we note an ENSO variance effect to sharpen the thermocline in the cold-tongue region. Other factors being equal, such a sharpening of the thermocline is expected to enhance the thermocline feedback supporting the growth of ENSO anomaly. Stability analyses (e.g. Jin 1998, Fedorov and Philander 2001) have indeed suggested that a warmer eastern Pacific with a moderately deeper thermocline tend to support a stronger ENSO activity. Elevated ENSO activity causes not only a deepening but also a sharpening of thermocline in the eastern Pacific, which in turn may further elevate ENSO activity.

The present study supports a positive feedback between ENSO variance and TPDV, and mechanisms for the phase transition of the ENSO variance cycle still remain unclear. Several possibility exist. During high ENSO-variance epochs, the above positive feedback may deepen the eastern thermocline so much so that ENSO may weaken or disappear entirely (Liang et al. 2012). The reduction in ENSO activity will lead to a weakened rectification effect, allowing the zonal SST gradient to strengthen as the system is restored towards its equilibrium state under the combined effect of radiative forcing and Bjerknes positive feedback (Liang et al. 2012). Hence "strong ENSO/positive TPDV" epoch turns into "weak ENSO/negative TPDV" epoch. An alternative, null hypothesis follows: TPDV arises simply due to nonlinear rectification of stochastically-forced ENSO variability. These hypotheses need to be tested with a hierarchy of models.

The present identification of a positive feedback between ENSO amplitude and TPDV helps explain why interdecadal modulation of ENSO amplitude has been prevalent over the past millennium (Li et al. 2011). To the extent that ENSO is the dominant mode at interannual variability, ENSO amplitude modulation has important implications for climate extreme occurrence around the globe.

Acknowledgements

We wish to thank Jinbao Li and Hiroki Tokinaga for constructive comments and suggestions. This research is supported by the National Science Foundation, and the Japan Agency for Marine-Earth Science and Technology (JAMSTEC) – International Pacific Research Center (IPRC) Initiative (JII) project. D.-.Z Sun was supported by climate and large-scale dynamics program of the US NSF (AGS 0852329). This is IPRC/SOEST publication #xxx/xxx.

Appendix A. Comparison in different OGCM responses

In this study, MOM version 3 (MOM3) is used for sensitivity experiments while the oceanic component of GFDL-CM2.1 is MOM version 4 (MOM4). There are some differences in horizontal and vertical resolution, mixing scheme, and surface boundary conditions. Comparison between MOM3 and MOM4 under the same boundary conditions, using Common Ocean-ice Reference Experiments version 2 (COREv2; Large and Yeager, 2008) forcing, is performed. The latter is obtained from the GFDL archive.

Figure A1 shows longitude-depth sections on the equator of temperature and zonal current velocity in MOM3 and MOM4. In zonal current on the equator, the westward surface current (about 100 cm/s) is stronger and the subsurface eastward equatorial under current (EUC; about 40 cm/s) is weaker in MOM3 than in MOM4. Horizontal and vertical resolution in MOM3 is coarser than MOM4 (see Section 2). In MOM3, the coarse meridional resolution slows down the EUC, resulting in a too weak deceleration of the westward surface current by vertical mixing. In MOM4, the explicit momentum transport by TIWs, through too weak compared to observations, may cause a weak surface current and off-equatorial maxima of surface westward current, in contrast to the equatorial maximum in MOM3 (not shown). A stronger westward current cools the warm pool temperature (about 2°C) in the western Pacific in MOM3 through temperature advection. Nevertheless, the overall structures of temperature and current (east-west thermocline slope and vertical stratifications, surface westward current and underlying EUC) are similar between MOM3 and MOM4. We note that Sun (2010, Plate 5) obtained a similar ENSO induced warming in the thermocline and surface cooling in the western Pacific in a different OGCM. Similar TPDV structure between epochs of high and low ENSO variance is found in CMIP3 models (Yu and Kim 2011), further suggesting that our results are not sensitive the choice of models. The similarity to MOM3 and MOM4 results indicates that the rectification pattern in this study is robust.

Appendix B. Heat budget analysis

Section 4b suggests that temperature advection and vertical diffusion are important for

ENSO rectification. Here we represent a detailed heat budget analysis. Figure A2 shows the difference between 2yrENSO and CTRL runs. Horizontal and vertical mixing terms are derived explicitly. In the western Pacific (0°N160°E), dynamical effect due to three-dimensional advection tends to cool in the upper 100m and vertical diffusion acts to damp this cooling tendency. In the lower layer (100-150m depth) of a warming signal in Fig. 8b, the dynamical effect is a warming effect while vertical diffusion rapidly decays. The strong vertical diffusion in the upper layer is consistent with the discussion in Section 4b. In the eastern Pacific (0°N250°E), the heat budget more complicated but there is an overall balance between dynamical advection and vertical mixing in the top 80m. In the lower thermocline (about 150-200m depth), the dynamical term acts to warm the subsurface water while the vertical diffusion rapidly decays in water deeper than 80m. These results from the heat budget analysis confirm that the dynamical term causes the ENSO rectification and the vertical diffusion effect is restricted in the mixed layer. The decomposition of the advection terms (Figure A3) shows that cooling (warming) due to the zonal (vertical) advection is significant in the western (eastern) tropical Pacific. These results are consistent with our discussion of Fig. 9.

References

An, S.-I., 2008 : Interannual Variations of the Tropical Ocean Instability Wave and ENSO, *J. Climate.* **21**, 3680-3686.

An, S.-I., 2009: A review on interdecadal changes in the nonlinearity of the El Niño–Southern Oscillation. *Theor. Appl. Climatol.*, **97,** 29–40.

Ashok, K., S. K. Behera, S. A. Rao, H. Weng, and T. Yamagata, 2007: El Niño Modoki and its possible teleconnection, *J. Geophys. Res.*, **112**, C11007, doi:10.1029/2006JC003798.

Anderson, W., A. Gnanadesikan, and A. Wittenberg, 2009: Regional impacts of ocean color on tropical Pacific variability. *Ocean Sci.*, **5**, 313-327.

Burgman, R. J., P. S. Schopf, B. P. Kirtman, 2008: Decadal Modulation of ENSO in a Hybrid Coupled Model. *J. Climate*, **21**, 5482–5500.

Choi, J., S.-I. An, B. Dewitte, W. W. Hsieh, 2009: Interactive Feedback between the Tropical Pacific Decadal Oscillation and ENSO in a Coupled General Circulation Model. *J. Climate*, **22**, 6597–6611.

Chowdary, J. S., S.-P. Xie, H. Tokinaga, Y. M. Okumura, H. Kubota, N. C. Johnson, and X.-T. Zheng, 2012: Inter-decadal variations in ENSO teleconnection to the Indo-western Pacific for 1870-2007. *J. Climate*, **25**, 1722–1744.

Collins, M., S.-I. An, W. Cai, A. Ganachaud, E. Guilyardi, F.-F. Jin, M. Jochum, M. Lengaigne, S. Power, A. Timmermann, G. Vecchi, and A. Wittenberg, 2010: The impact of global warming on the tropical Pacific and El Niño. *Nature Geoscience*, **3**, 391-397. doi:10.1038/ngeo868

Delworth, T. L., and coauthors, 2006: GFDL's CM2 global coupled climate models, Part I: Formulation and simulation characteristics. *J. Climate*, **19**, 643-674.

DiNezio, P. N., B. P. Kirtman, A. C. Clement, S.-K. Lee, G. A. Vecchi, and A. Wittenberg, 2012: Mean climate controls on the simulated response of ENSO to increasing greenhouse gases. *J. Climate*, in press. doi: 10.1175/JCLI-D-11-00494.1

Fang, Y., J. C. H. Chiang, and P. Chang, 2008: Variation of mean sea surface temperature and modulation of El Niño–Southern Oscillation variance during the past 150 years, *Geophys. Res. Lett.*, **35**, L14709, doi:10.1029/2008GL033761.

Fedorov, A. V., and S. G. H. Philander, 2001: A stability analysis of tropical ocean–atmosphere interactions: Bridging measurements and theory for El Niño. *J. Climate*, **14,** 3086–3101.

GAMDT, 2004: The new GFDL global atmosphere and land model AM2/CM2.0: Evaluation with prescribed SST simulations. *J. Climate.* **17**, 4641–4673.

Gebbie, G., I. Eisenman, A. Wittenberg, and E. Tziperman, 2007: Modulation of westerly wind bursts by sea surface temperature: A semistochastic feedback for ENSO. *J. Atmos. Sci.*, **64,** 3281–3295.

Gent, P.R., and J. C. McWilliams, 1990: Isopycnal mixing in ocean circulation models. *J. Phys. Oceanogr.*, **20**, 150–155.

Gnanadesikan, A., and coauthors, 2006: GFDL's CM2 global coupled climate models, Part II: The baseline ocean simulation. *J. Climate*, **19**, 675-697

Griffies, S. M., 1998: The Gent-McWilliams skew flux. *J. Phys. Oceanogr.*, **28**, 831-841.

Griffies, S. M., A. Guanadesikan, R. C. Pacanowski, V. D. Larichev, J. K. Dukowicz, and R. D. Smith, 1998: Isoneutral diffusion in a z-coordinate ocean model. *J. Phys. Oceanogr.*, **28**, 805–830.

Griffies, S. M., and Coauthors, 2005: Formulation of an ocean model for global climate simulations. *Ocean Sci.*, **1.** 45-79.

Guilyardi, E., A. Wittenberg, A. Fedorov, M. Collins, C. Wang, A. Capotondi, G. J. van Oldenborgh, and T. Stockdale, 2009: Understanding El Niño in ocean-atmosphere general circulation models: Progress and challenges. Bull. Amer. Meteor. Soc., 90, 325-340. doi:10.1175/2008BAMS2387.1

Guilyardi, E., W. Cai, M. Collins, A. Fedorov, F.-F. Jin, A. Kumar, D.-Z. Sun, and A. Wittenberg, 2012: New strategies for evaluating ENSO processes in climate models. *Bull. Amer. Met. Soc.*, **93**, 235-238. doi: 10.1175/BAM S-D-11-00106.1

Horel, J. D., and J. M. Wallace, 1981: Planetary-scale atmospheric phenomena associated with the Southern Oscillation. *Mon. Wea. Rev.*, **109**, 813–829.

Jin, F-F., 1998: A simple model for the Pacific cold tongue and ENSO. *J. Atmos. Sci.*, **55,** 2458–2469.

Kao, H.-Y., and J.-Y. Yu, 2009: Contrasting eastern-Pacific and central-Pacific types of ENSO, *J. Clim*., **22**, 615–632, doi:10.1175/ 2008JCLI2309.1.

Kalnay, E., and Coauthors, 1996: The NCEP/NCAR 40-Year Reanalysis Project. *Bull. Amer. Meteor. Soc*, **77,** 437–471.

Kessler, W. S., and R. Kleeman, 2000: Rectification of the Madden–Julian oscillation into the ENSO cycle. *J. Climate*, **13,** 3560–3575.

Kirtman, B. P., and P. S. Schopf, 1998: Decadal variability in ENSO predictability and prediction. *J. Climate*, **11**, 2804-2822.

Kug, J-S., J. Choi, S-I. An, F-F. Jin, A. T. Wittenberg, 2010: Warm Pool and Cold Tongue El Niño Events as Simulated by the GFDL 2.1 Coupled GCM. *J. Climate*, **23**, 1226–1239.

Large, W. G., J. C. McWilliams, and S. C. Doney, 1994: Oceanic vertical mixing: A review and a model with a nonlocal boundary layer parameterization. *Rev. Geophys*., **32,** 363-403.

Li, J., S.-P. Xie, E. R. Cook, G. Huang, R. D'Arrigo, F. Liu, J. Ma and X. Zheng, 2011: Interdecadal modulation of El Nino amplitude during the past millennium. *Nature Climate Change*, **1**, 114-118.

Liang, J., X.-Q. Yang and D.-Z. Sun, 2012: The Effect of ENSO Events on the Tropical Pacific Mean Climate: Insights from an Analytical Model. *J. Climate*, in revision.

Lin, S-J., 2004: A "vertically Lagrangian" finite-volume dynamical core for global models. *Mon. Wea. Rev.,* **132,** 2293-2307.

McPhaden, M. J., T. Lee, and D. McClurg, 2011: El Niño and its relationship to changing background conditions in the tropical Pacific Ocean, *Geophys. Res. Lett.*, **38**, L15709, doi:10.1029/2011GL048275.

Moorthi, S., and M. J. Suarez, 1992: Relaxed Arakawa-Schubert: A parameterization of moist convection for general circulation models. *Mon. Wea. Rev.,* **120,** 978-1002.

Morioka Y., T. Tozuka, and T. Yamagata, 2011: On the growth and decay of the subtropical dipole mode in the South Atlantic. *J. Climate*, doi: 10.1175/2011JCLI 4010.1

Ohba, M., and H. Ueda, 2009: Role of Nonlinear Atmospheric Response to SST on the Asymmetric Transition Process of ENSO. *J. Climate*, **22**, 177-192.

Ohba, M., 2012: Important factors for the decadal change of ENSO transitivity and persistency. *Inter. J. Clim.*,**32,** DOI: 10.1002/joc.3529.

Okumura Y.M., M. Ohba, C. Deser, and H. Ueda, 2011: A proposed mechanism for the asymmetric duration of El Nino and La Nina. *J. Climate*, **24**, 3822-3829.

Pacanowski, R. C., and S. G. H. Philander, 1981: Parameterization of vertical mixing in numerical models of tropical oceans. *J. Phys. Oceanogr.*, **11**, 1443-1451.

Pacanowski, R. C., and S. M. Griffies, 1999: MOM3.0 manual. *NOAA/GFDL*, pp 680.

Rodgers, K. B., P. Friederichs, and M. Latif, 2004: Tropical Pacific decadal variability and its relation to decadal modulations of ENSO. *J. Climate*, **17,** 3761–3774.

Rosati, A., K. Miyakoda, 1988: A General Circulation Model for Upper Ocean Simulation. *J. Phys. Oceanogr.*, **18**, 1601–1626.

Schopf, P. S., and R. J. Burgman, 2006: A simple mechanism for ENSO residuals and asymmetry. *J. Climate*, **19,** 3167–3179.

Smith, T. M., R. W. Reynolds, T. C. Peterson, J. Lawrimore, 2008: Improvements to NOAA's Historical Merged Land–Ocean Surface Temperature Analysis (1880–2006). *J. Climate*, **21**, 2283–2296.

Sun, D.-Z. and T. Zhang, 2006: A Regulatory Effect of ENSO on the Time-Mean Thermal Stratification of the Equatorial Upper Ocean. *Geophys. Res. Lett.*, **33**, L07710, doi:10.1029/2005GL025296.

Sun, D.-Z., 2010: The Diabatic and Nonlinear Aspects of El Nino Southern Oscillation: Implications for its Past and Future Behavior, in *AGU Geophysical Monograph "Climate Dynamics: Why Does Climate Vary?"*, edited by D.-Z. Sun and F. Bryan, pp 79-104.

Sun, D.-Z., T. Zhang, Y. Sun, and Y. Yu, 2012: Rectification of El Nino-Southern Oscillation into Climate Anomalies of Decadal and Longer Time-scales. *J. Climate*, Submitted.

Sun, F., and J.-Y. Yu, 2009: A 10–15-yr modulation cycle of ENSO intensity. *J. Climate*, **22**, 1718–1735.

Suzuki T., and K. Takeuchi, 2000: Response of Equatorial Pacific Mean Temperature Field to Intraseasonal Wind Forcing. *J. Oceanogr.,* **56** (5), 485-494.

Timmermann, A., 2003: Decadal ENSO amplitude modulations: A nonlinear paradigm. *Global Planet. Change*, **37,** 135–156.

Tozuka T., T. Yokoi, and T. Yamagata, 2010: A modeling study of interannual variations of the Seychelles Dome. *J. Geophys. Res.*, ***115***, C04005, doi:10.1029/2009 JC005547.

Vecchi, G. A., and A. T. Wittenberg, 2010: El Niño and our future climate: Where do we stand? *Wiley Interdisciplinary Reviews: Climate Change*, 1, 260-270. doi:10.1002/wcc.33

Walker, G. T., 1923: Correlation in seasonal variations of weather VIII. A preliminary study of world weather. *Mem. Indian Meteorol. Dep.*, **24**(4), 75-131.

Watanabe, M., and A. T. Wittenberg, 2012: A method for disentangling El Niño-mean state interaction. Geophys. Res. Lett., 39, L14702. doi:10.1029/2012GL052013

Watanabe, M., J.-S. Kug, F.-F. Jin, M. Collins, M. Ohba, and A. T. Wittenberg, 2012: Uncertainty in the ENSO amplitude change from the past to the future. Geophys. Res. Lett., in press. doi :10.1029/2012GL053305

Wittenberg, A. T., 2002: ENSO response to altered climates. Ph.D. thesis, Princeton University. 475pp.

Wittenberg, A. T., 2004: Extended wind stress analyses for ENSO. *J. Climate*, **17**, 2526-2540.

Wittenberg, A. T., A. Rosati, N.-C. Lau, and J. J. Ploshay, 2006: GFDL's CM2 global coupled climate models. Part III: Tropical Pacific climate and ENSO. *J. Climate*, **19**, 698-722.

Wittenberg, A. T., 2009: Are historical records sufficient to constrain ENSO simulations?, *Geophys. Res. Lett.*, ***36***, L12702, doi:10.1029/2009GL038710.

Xie, S.-P., Y. Du, G. Huang, X.-T. Zheng, H. Tokinaga, K. Hu, and Q. Liu, 2010: Decadal shift in El Nino influences on Indo-western Pacific and East Asian climate in the 1970s. *J. Climate*, **23**, 3352-3368.

Yu, J.-Y., S.-T. Kim, 2011: Reversed Spatial Asymmetries between El Niño and La Niña and Their Linkage to Decadal ENSO Modulation in CMIP3 Models. *J. Climate*, **24**, 5423–5434.

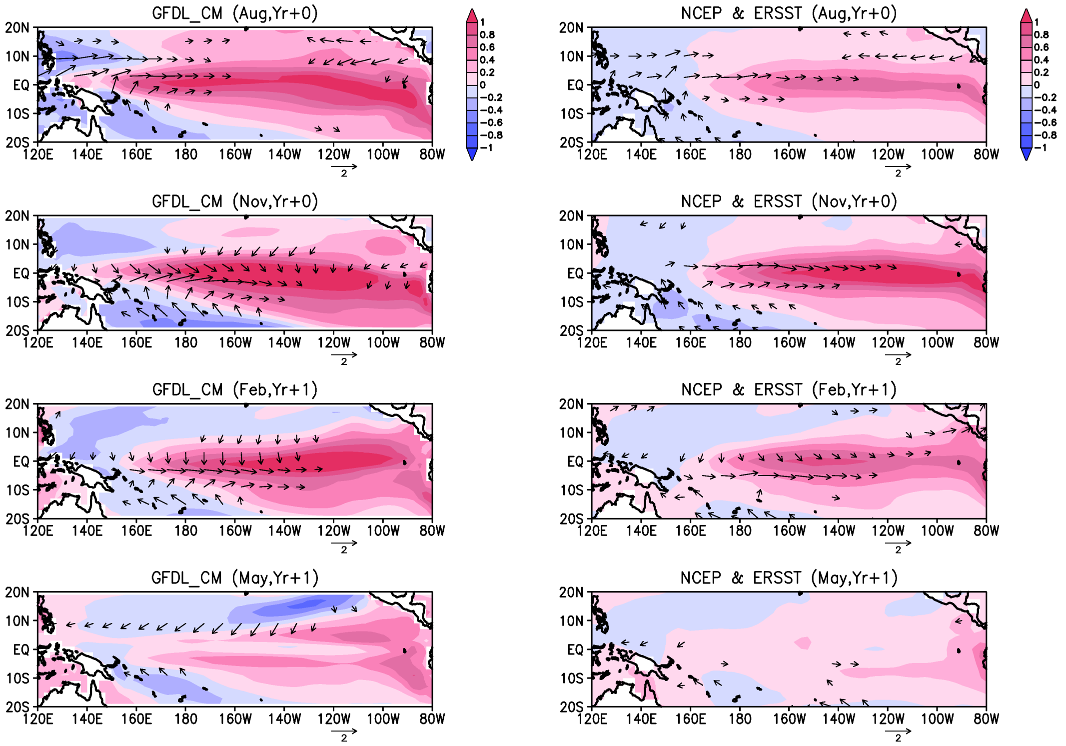

Figure 1: Seasonal march of composite ENSO. SST (°C) and surface wind (m/s) in CM2.1 simulation (left) and observation (right). Each variables are normalized by Nino-3 SSTA (2.2°C in CM2.1, and 1.4°C in ERSST) and Nino-4 zonal wind anomaly (2.8 m/s in CM2.1, and 1.8 m/s in NCEP) during December-February.

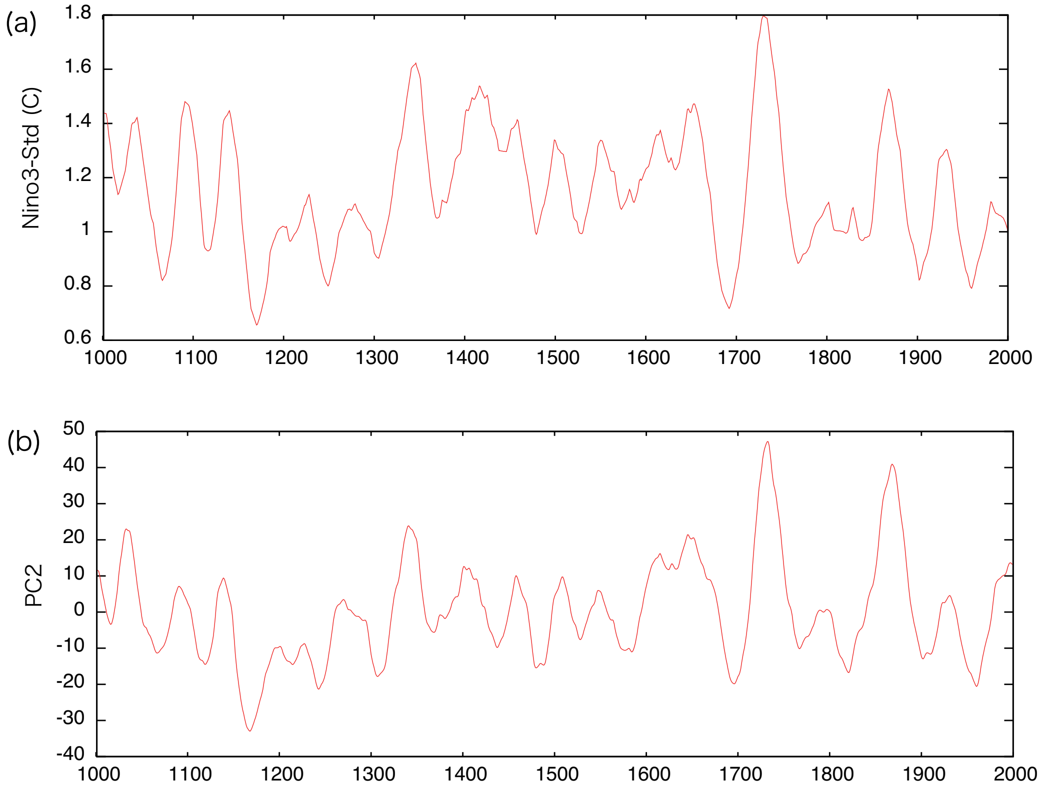

Figure 2: Time series of CM2.1 simulated (a) 20 year sliding standard deviation of Nino-3 index, and (b) second TPDV mode for the last 1000 years.

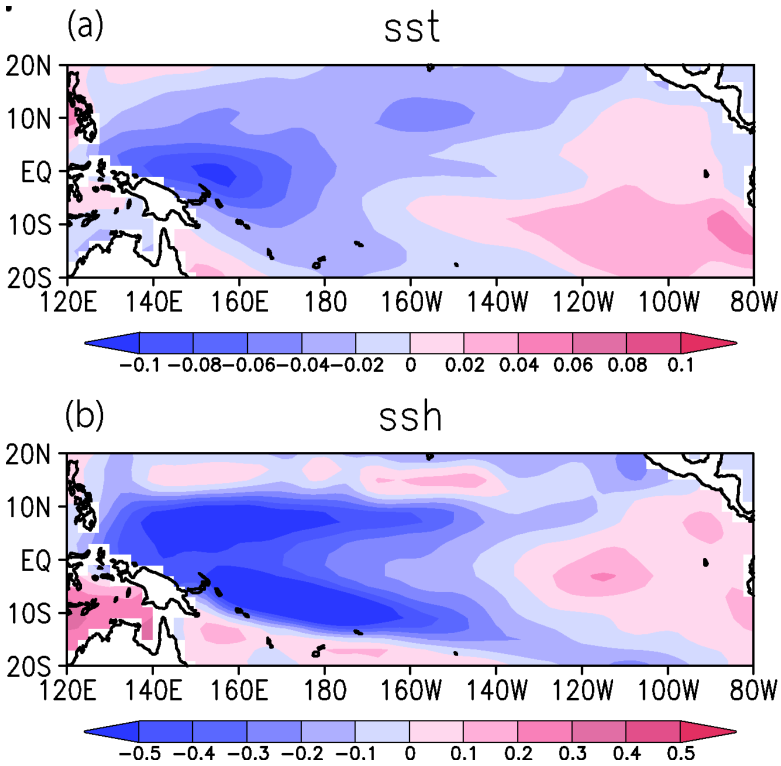

Figure 3: Regression pattern of the 20 year low-passed (a) SST (°C) and (b) SSH (cm) anomaly field onto 20 year low-passed ENSO variance index.

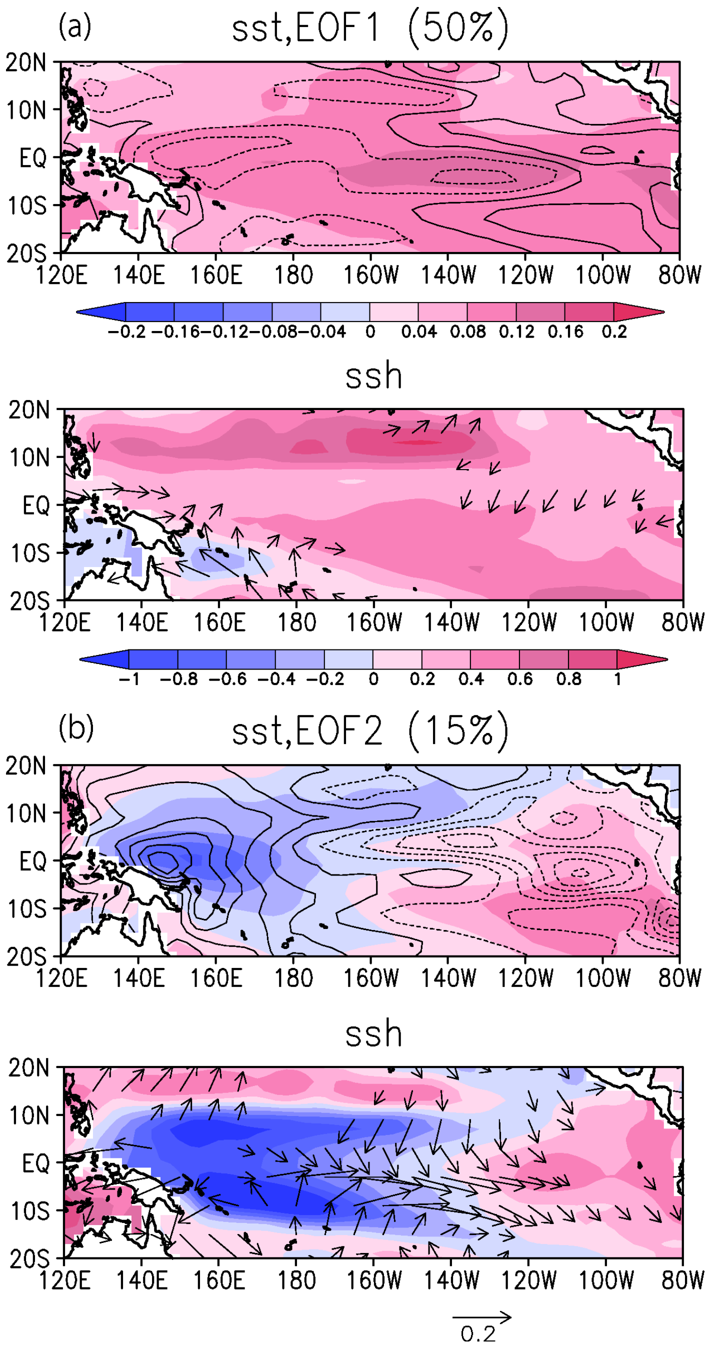

Figure 4: Spatial SST (upper, °C) and SSH (lower, cm) anomaly pattern for (a) first TPDV and (b) second TPDV mode. Surface heat flux (contour intervals at 0.1 W/m^2; positive downward) and surface wind (right in vector, m/s) are superposed. Variables expect SST are regressed onto the SST PCs.

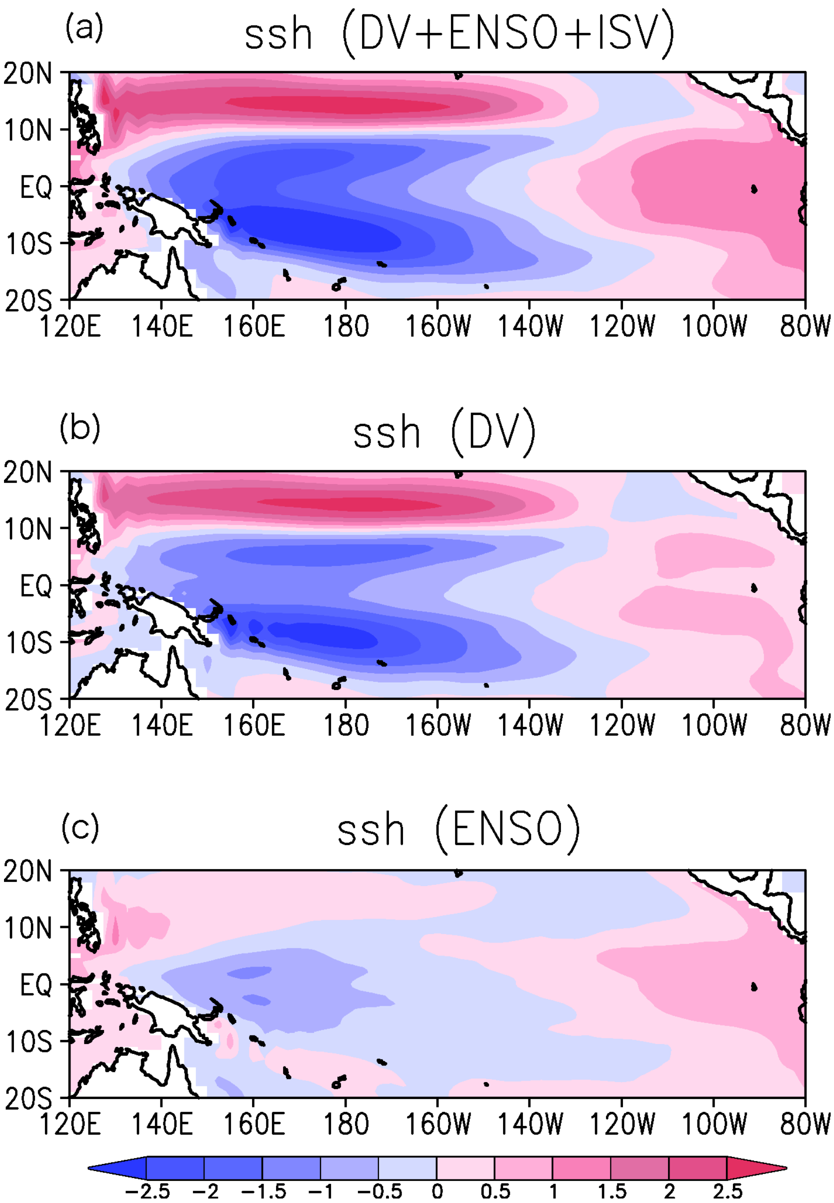

Figure 5: OGCM simulated decadal SSH responses (cm) to strong-ENSO minus weak-ENSO epochs for (a) DV+ENSO+ISV, (b) DV runs and (c) contribution of ENSO.

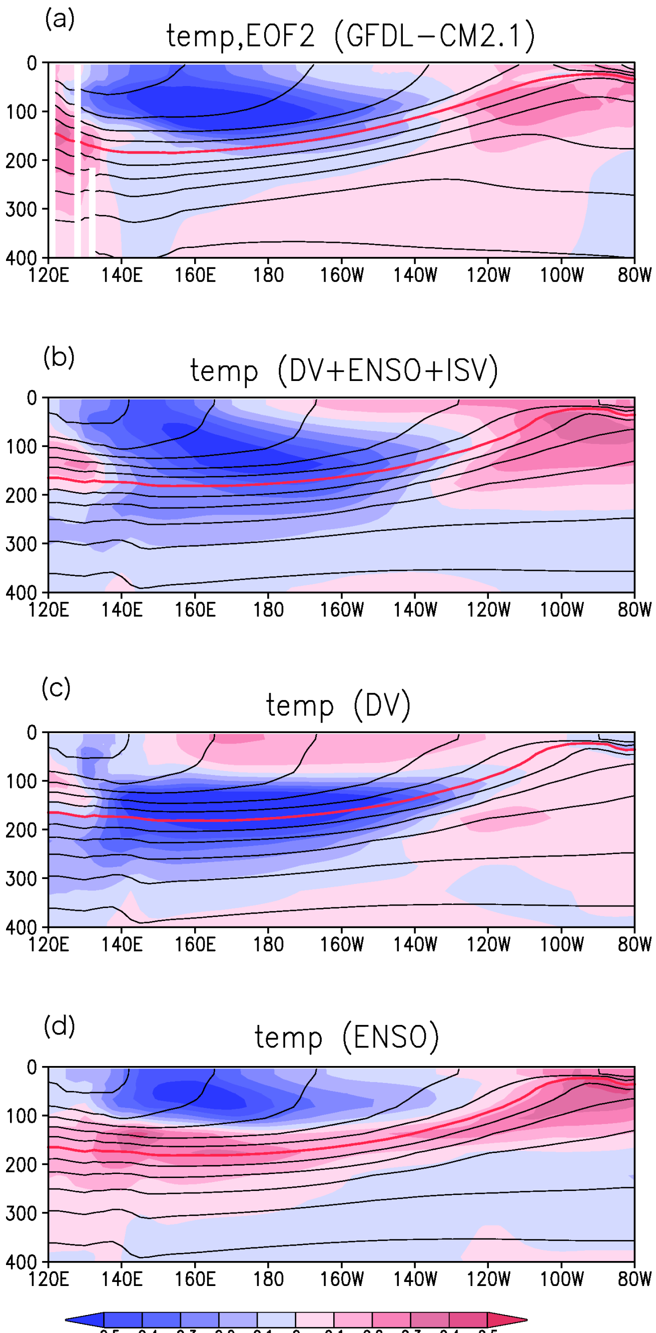

Figure 6: (a) second TPDV mode of temperature anomaly (°C) on the equator in CM2.1. OGCM simulated temperature responses on the equator for (b) DV+ENSO+ISV, (c) DV runs and (d) contribution of ENSO. Contour interval of mean temperature is 2°C and red contour shows 20°C isotherm.

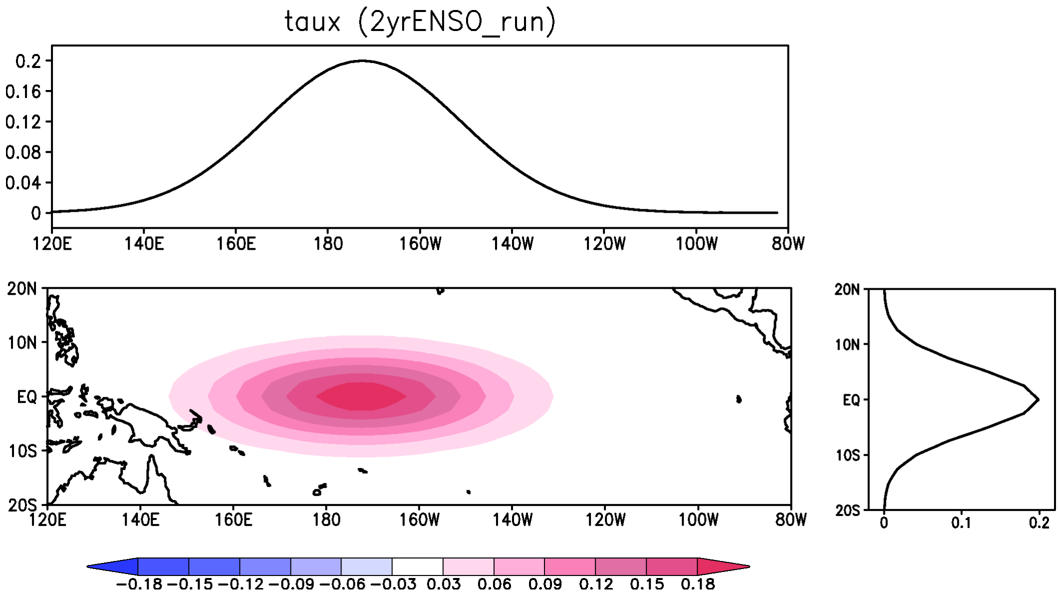

Figure 7: Spatial pattern of imposed zonal wind stress anomaly (dyn/cm^2) in 2yrENSO run (lower left). Longitude section on the equator (upper) and latitude section at 190°E (lower right) are also shown.

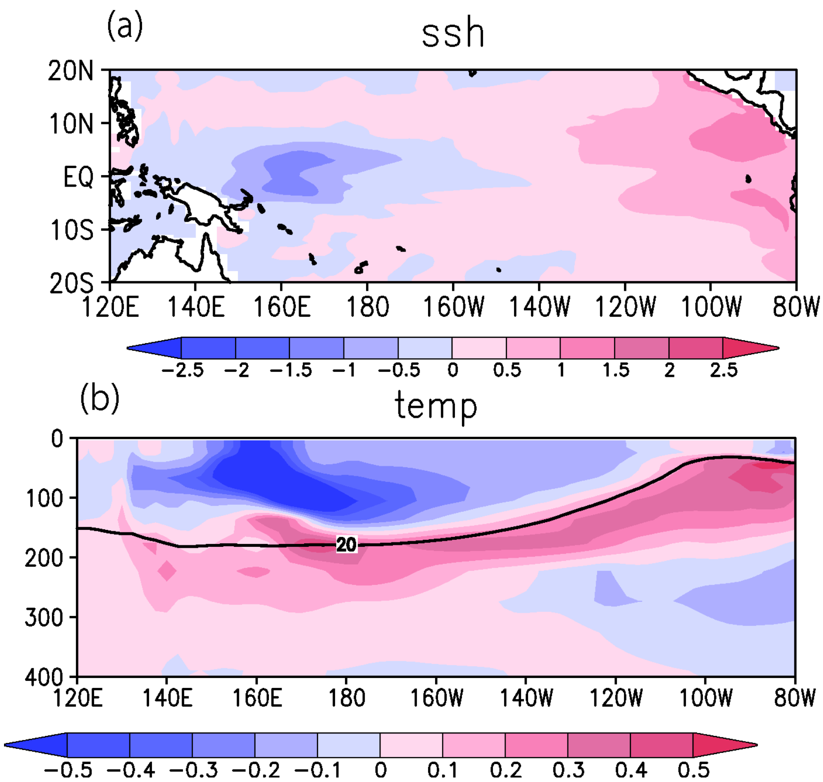

Figure 8: Response to idealized periodic ENSO forcing defined by difference between 2yrENSO and CTRL run, (a) SSH difference (cm) and (b) temperature difference on the equator (°C)

Rendered Figure 9

Click here to download Rendered Figure: fig9_25oct2012.pdf

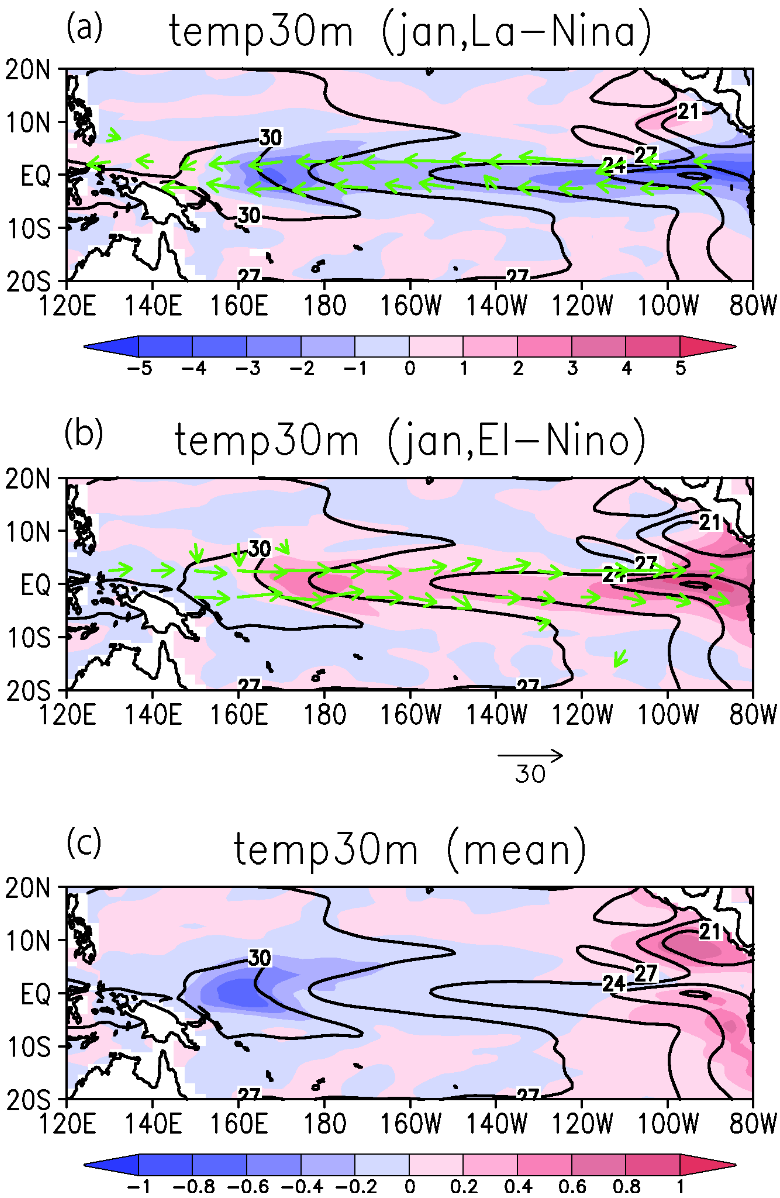

Figure 9: Response to idealized 2 year periodic ENSO forcing defined by difference between 2yrENSO and CTRL run, 30m temperature difference (shaded, °C) and current difference (vector, cm/s) during (a) La-Nina like period, (b) El-Nino like period and (c) mean temperature response. Mean SST in CTRL run is superposed in contour.

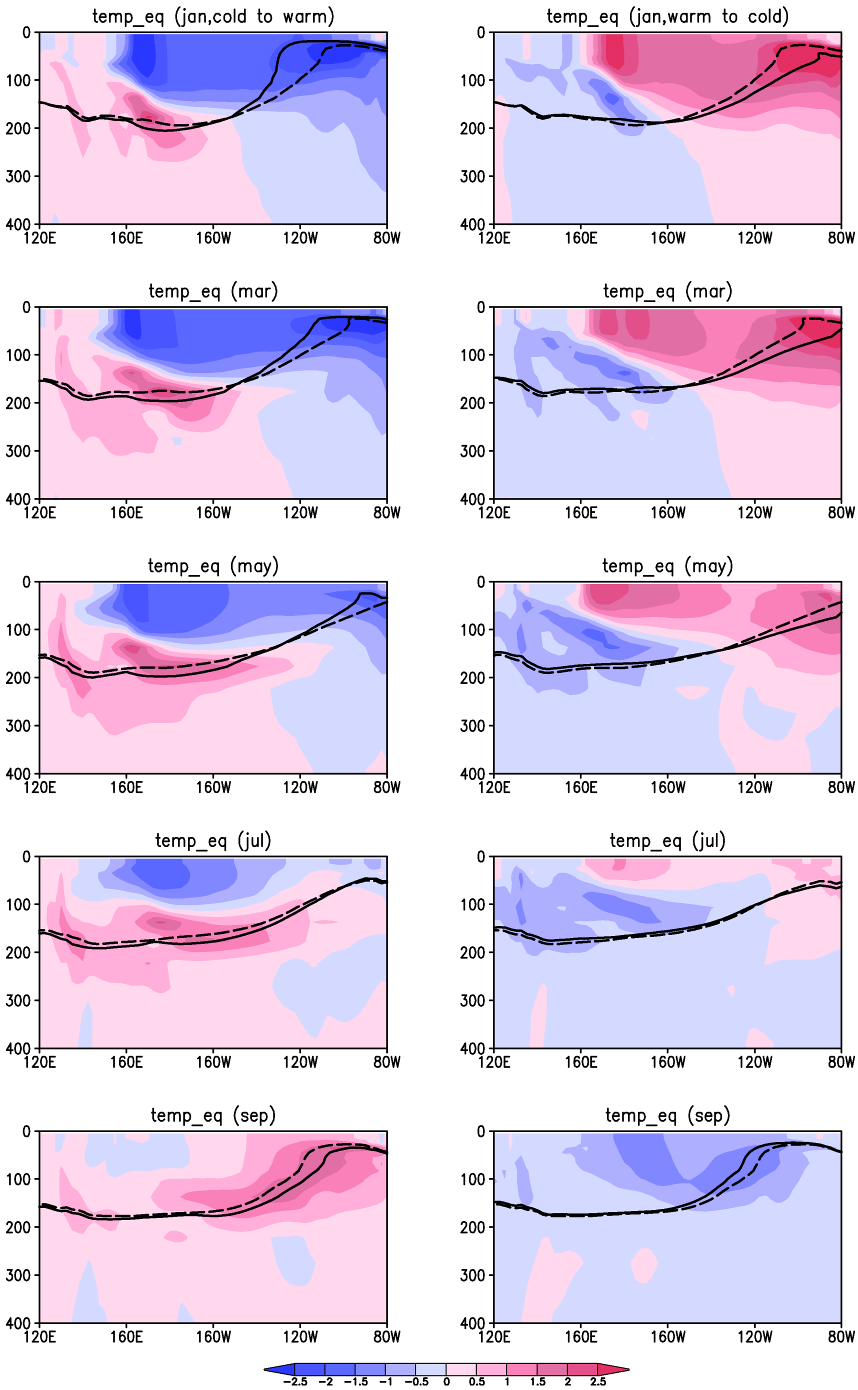

Figure 10: Time series of temperature response (°C) on the equator during easterly to westerly phase (left) and westerly to easterly phase (right). The 20°C isotherm in 2yrENSO (CTRL) run is superposed in solid (dashed) contour.

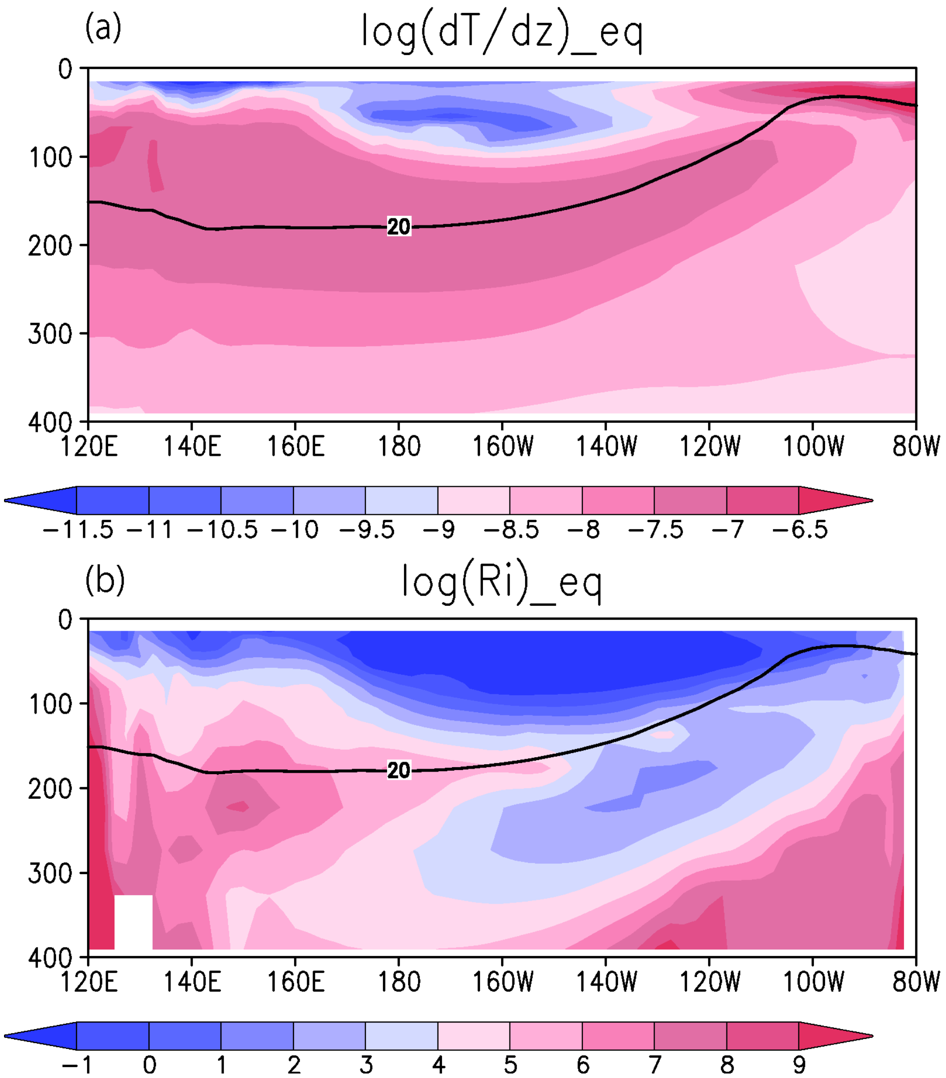

Figure 11: Longitude-depth section on the equator of the log-scaled (a) vertical temperature gradient and (b) Richardson number. Richardson number is calculated from 5-day snapshot, and then mean value is derived.

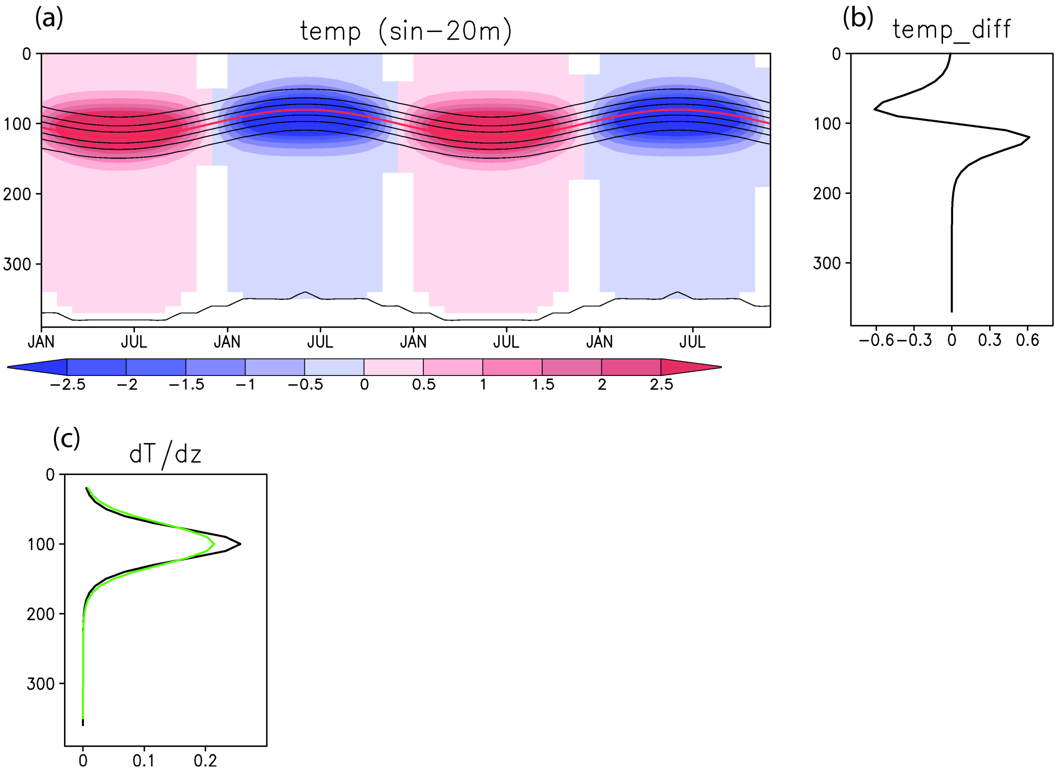

Figure 12: (a) Depth-time section of idealized *tanh(z)* type thermocline variability (contour, °C) and its difference from a Lagrangian snapshot without vertical displacement (shaded, °C). (b) Temperature difference defined by Eulerian mean temperature minus Lagrangian snapshot. (c) *dT/dz* (°C/m) in Eulerian mean (green) and Lagrangian snapshot (black). In (a), red contour shows 20°C isotherm. Idealized thermocline $T(z,t)$ is assumed as $T(z,t)=28-16(1+\tanh(z-z_0(t)/H_0))/2$ (°C), $z_0(t)=100-20\sin(2\pi t/24)$ (m), $H_0=30$ (m).

Rendered Figure 13
Click here to download Rendered Figure: fig13_25oct2012.pdf

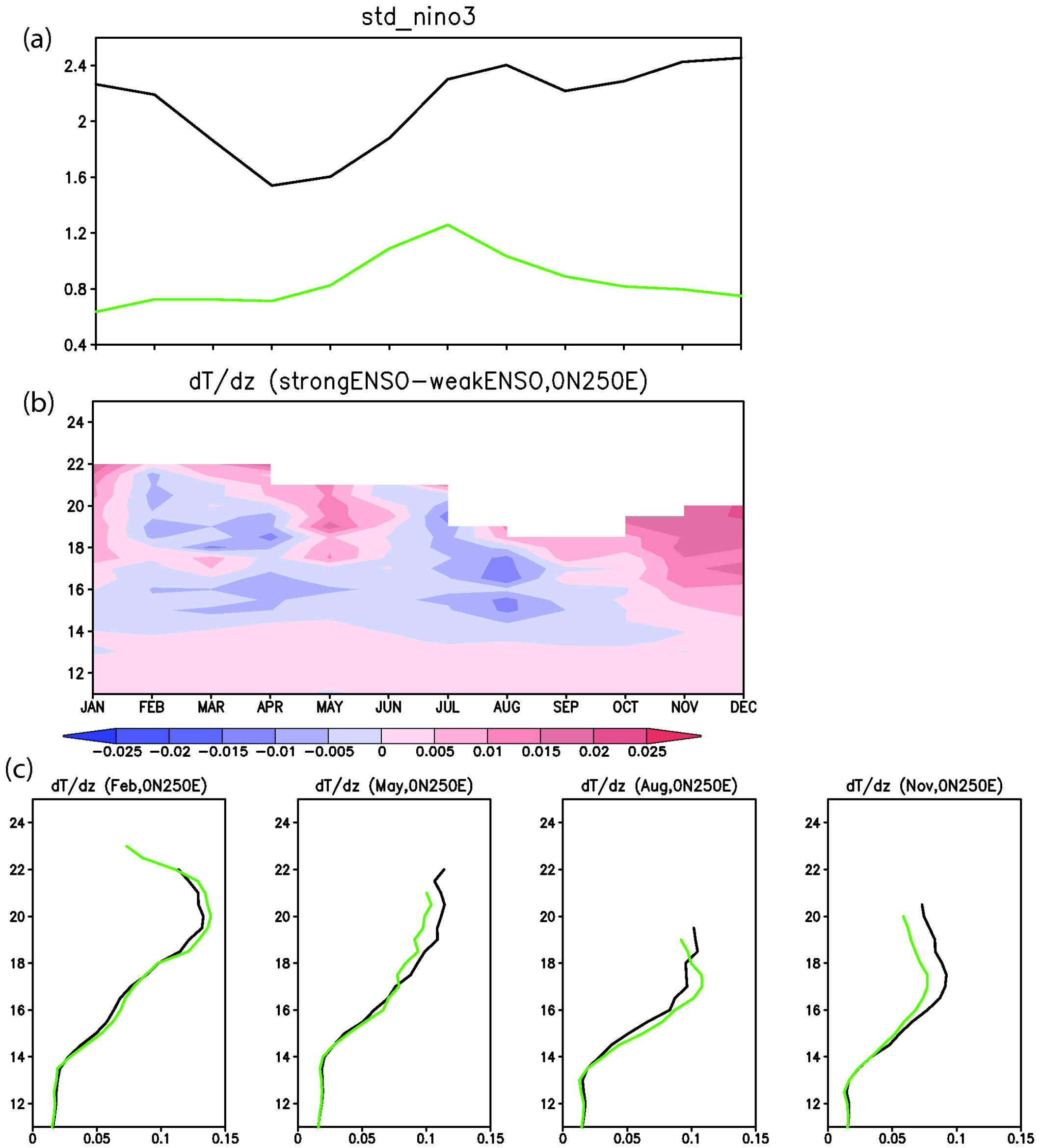

Figure 13: (a) Monthly standard deviation of SST anomaly over the Nino-3 region (°C) in "strong ENSO/positive TPDV" epochs (black) and "weak ENSO/negative TPDV" epochs (green) in CM2.1 simulation. (b) Temperature-time section of *dT/dz* difference (°C/m) defined by "strong ENSO/positive TPDV" epochs minus "weak ENSO/negative TPDV" epochs at 0°N250°E. (c) *dT/dz* (°C/m) in "weak ENSO/negative TPDV" epochs (green) and "strong ENSO/positive TPDV" epochs (black).

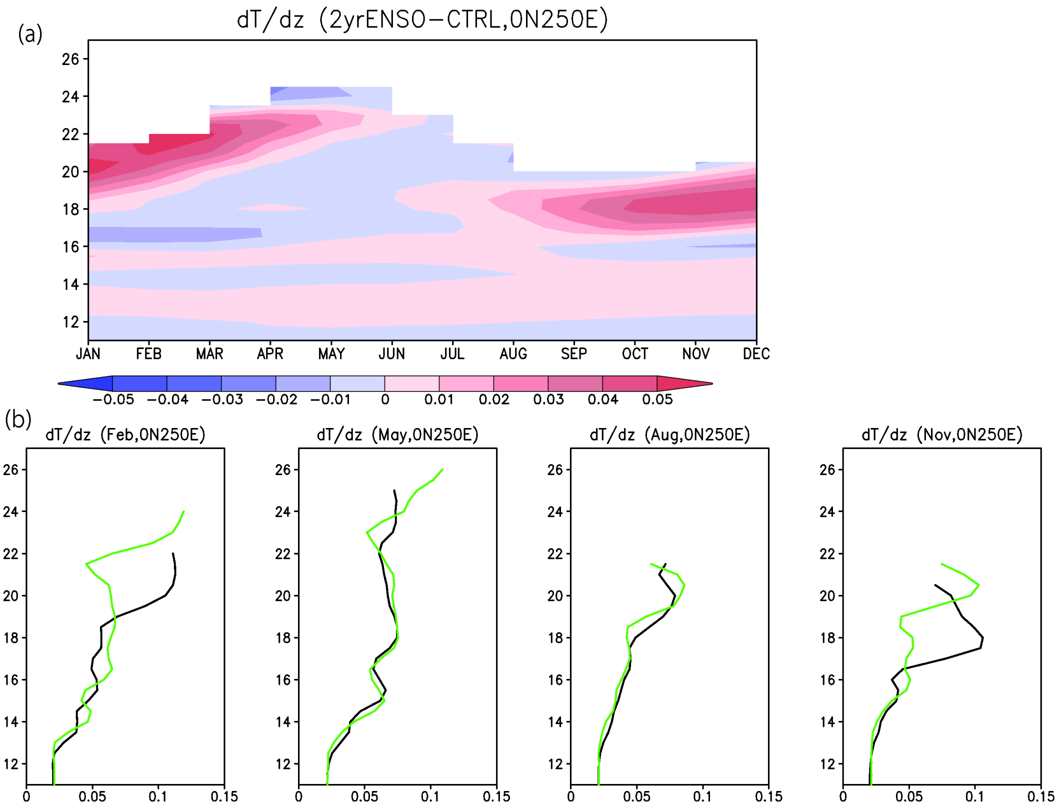

Figure 14: (a) Temperature-time section of *dT/dz* difference (°C/m) defined by 2yrENSO run minus CTRL run in OGCM sensitivity experiments at 0°N250°E. (b) *dT/dz* (°C/m) in CTRL run (green) and 2yrENSO run (black).

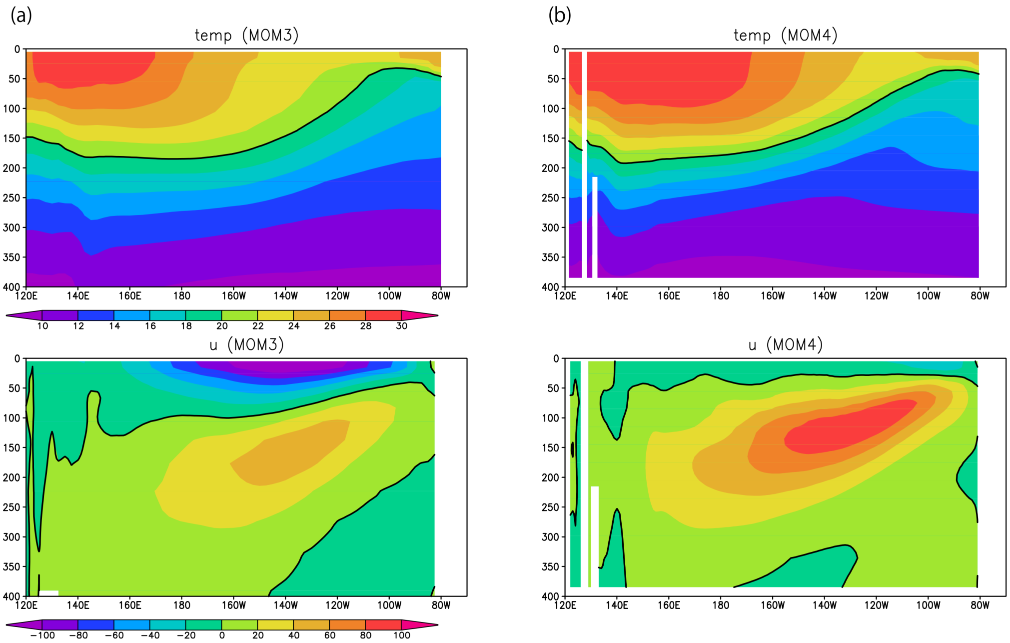

Figure A1: Longitude-depth section on the equator of temperature (upper: °C) and zonal current velocity (lower: cm/s) in (a) MOM3 and (b) MOM4 experiments forced by COREv2 normal-year forcing.

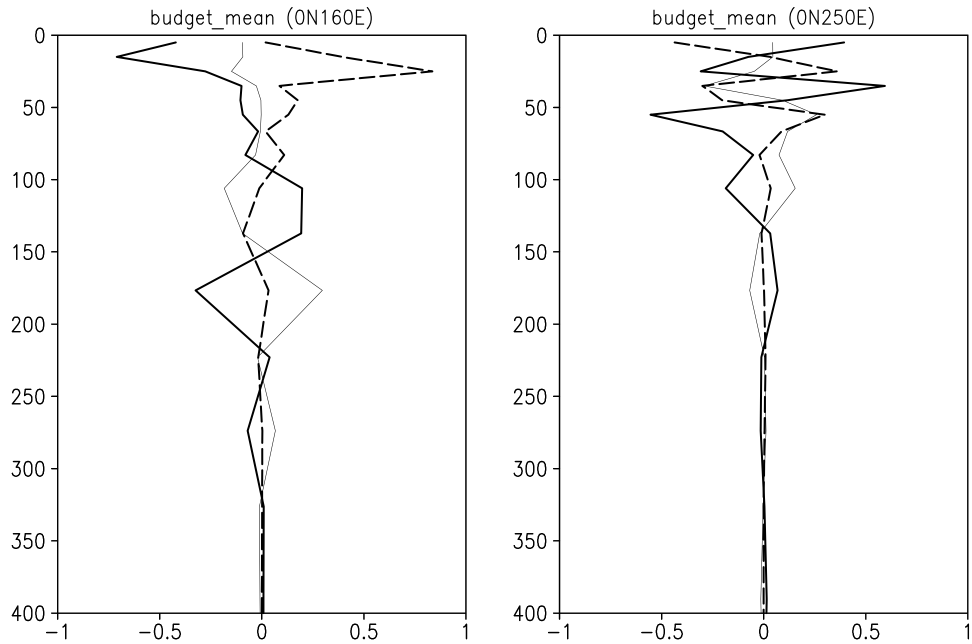

Figure A2: Heat budget terms (10^{-7} °C/s) in the difference between 2yrENSO and CTRL runs (2yrENSO-CTRL) at (a) 0°N160°E and (b) 0°N250°E. Three dimensional dynamical advection (thick line), horizontal diffusion (thin line), and vertical diffusion (thick dashed).

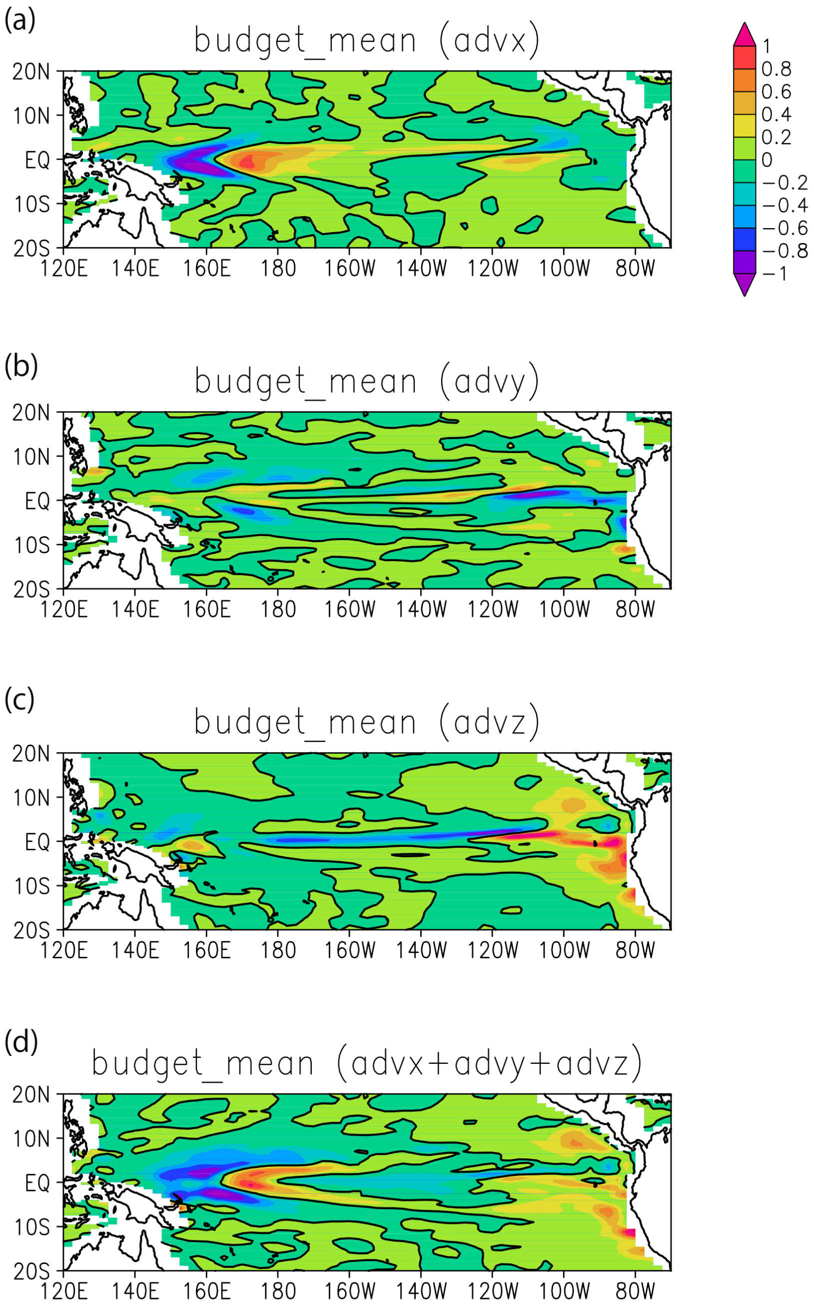

Figure A3: Horizontal distribution of advection terms (10^{-7} °C/s) as the difference between 2yrENSO and CTRL runs (2yrENSO-CTRL) in the upper 50m. (a) zonal advection (advx), (b) meridional advection (advy), (c) vertical advection (advz) and (d) these sum (advx+advy+advz).